https://doi.org/10.5194/egusphere-2026-3431
Preprint. Discussion started: 25 June 2026

A low-dimensional framework for interpreting Northern Hemisphere winter extratropical precipitation trends

Ha-Rim Kim[1], Changhyun Yoo[2*], Hyodae Seo[3], and Baek-Min Kim[4]

[1]Institute of Sustainable Earth and Environmental Dynamics, Pukyong National University, Busan, 48513, Republic of Korea
[2]Department of Climate and Energy Systems Engineering, Ewha Womans University, Seoul, 03760, Republic of Korea
[3]Department of Oceanography, University of Hawai'i at Manoa, Honolulu, HI 96822, USA
[4]Division of Earth Environmental System Science, Pukyong National University, Busan, 48513, Republic of Korea

Correspondence to: Changhyun Yoo (cyoo@ewha.ac.kr)

Abstract. Extratropical precipitation trends are strongly affected by changes in large-scale circulation, but the relevant dynamic signals are often difficult to isolate in climate models. Here, we introduce a low-dimensional framework that reconstructs Northern Hemisphere winter precipitation trends from leading modes of 500-hPa geopotential-height variability. The framework decomposes circulation variability into transient, stationary, and interaction components, and links their EOF modes to precipitation using ERA5 and CMIP6 historical and SSP5-8.5 simulations. In ERA5, the leading circulation modes reproduce much of the observed precipitation redistribution, with drying in the subtropics and wetting in the midlatitudes. The transient storm-track component dominates the reconstruction, with shift and sharpening modes accounting for most of the circulation-linked precipitation trend. CMIP6 models capture the broad meridional structure of this response but underestimate its amplitude. The weak multi-model mean response results from large intermodel spread and sign cancellation in the pulsing and shift modes, while the sharpening mode remains more coherent across models. Under SSP5-8.5, circulation-induced precipitation trends become weaker relative to total precipitation trends, consistent with an increasing role of thermodynamic moistening. Nevertheless, the spatial structure of precipitation change remains strongly tied to storm-track variability. These results suggest that uncertainty in future extratropical precipitation redistribution depends not only on the magnitude of warming but also on how models represent the modal structure of storm-track change and its coupling to precipitation.

1 Introduction

The large-scale distribution of midlatitude precipitation and its response to global warming are commonly interpreted in terms of thermodynamic and dynamic contributions. From a moisture budget perspective, thermodynamic change reflects increases in water vapor under approximately constant relative humidity (Trenberth et al., 2003; Held and Soden 2006), whereas dynamic change arises from circulation-driven changes in moisture transport and its convergence (Seager et al. 2010). In the extratropics, these circulation effects are mediated by eddy activity across timescales, from

https://doi.org/10.5194/egusphere-2026-3431
Preprint. Discussion started: 25 June 2026

synoptic transient eddies to lower-frequency, stationary circulation anomalies. Transient eddies make a major contribution to extratropical moisture transport and moisture-flux convergence, thereby shaping precipitation variability (Peixoto and Oort 1992; Newman et al. 2012), while stationary anomalies modify the background flow and can modulate storm development and precipitation (Lau 1988; Seager et al. 2014; Simpson et al. 2016). Consequently, uncertainty in the forced response of midlatitude circulation variability remains a major source of uncertainty in projections of extratropical precipitation change (e.g., Zappa et al. 2013; Shaw et al. 2016; Harvey et al. 2020; Simpson et al. 2021).

A key challenge, therefore, is to describe circulation-related precipitation trends in a way that is both physically interpretable and sufficiently compact for attribution and model comparison. Eulerian storm-track diagnostics provide a useful practical starting point because they quantify variance in geopotential height or related measures such as eddy kinetic energy (e.g., Blackmon et al. 1984; Lau 1988). However, by construction, these diagnostics primarily emphasize transient variability, making it less straightforward to interpret the combined contributions of transient eddies, stationary circulation variability, and their interactions within a single framework. This motivates the development of a framework capable of attributing precipitation variability and trends across multiple timescales, spanning synoptic disturbances to quasi-stationary circulation variability. Moreover, much of the variability of Eulerian storm-track measures can be captured by a small number of empirical orthogonal functions (EOFs), which are often interpreted as changes in amplitude ("pulsing"), meridional position ("shifting"), and broader reorganization (Wettstein and Wallace 2010). Recent work shows that storm-track EOF modes provide a skillful basis for diagnosing associated extratropical precipitation variability (Deng and Jiang 2011; Yoo et al. 2025). For example, Yoo et al. (2025) used an EOF decomposition of storm-track variability to show that leading storm-track modes map onto distinct, coherent precipitation anomaly patterns, linking specific storm-track EOFs to characteristic precipitation responses.

Building on these ideas, we develop an EOF-based reconstruction framework to attribute observed multidecadal precipitation trends to a small set of leading modes of atmospheric variability. This framework is also motivated by persistent uncertainty in circulation responses to forcing across generations of climate models. While a poleward shift of extratropical storm tracks has been noted since the CMIP3 era (Yin 2005), CMIP5 and CMIP6 exhibit substantial spread in the magnitude and structure of circulation reorganization (Chang et al. 2012; Barnes and Polvani 2013; Zappa et al. 2013; Harvey et al. 2020; Simpson et al. 2021), with recent observational constraints indicating that models may systematically underestimate poleward shifts in storm tracks (Chemke and Yuval 2026). In this context, an EOF-based framework provides a compact basis for model evaluation: it tests whether models reproduce the observed leading storm-track patterns, their historical evolution, and the associated precipitation signatures inferred from reanalysis. Framing model behavior within this reduced-dimensional space also facilitates diagnosis of the sources of intermodel spread by separating differences in the storm-track mode structure, the historical evolution of mode amplitudes, and the precipitation response associated with a given mode, rather than relying only on bulk measures such as storm-track shifts or intensity changes.

https://doi.org/10.5194/egusphere-2026-3431
Preprint. Discussion started: 25 June 2026

Motivated by these considerations, we ask whether and to what extent differences in CMIP6 precipitation projections can be understood in terms of low-dimensional changes in atmospheric variability modes and their associated precipitation signatures. Specifically, we address the following questions:

1. What fraction of the observed multidecadal DJF precipitation trend in ERA5 can be explained by a small number of leading EOF modes, and how do the stationary, transient, and interaction components contribute?
2. How do the storm-track-mode-based reconstructed precipitation trends compare between ERA5 and CMIP6, and where do models systematically diverge from the observed reconstruction?
3. Which modes contribute most to the intermodel spread in reconstructed precipitation trends, and through what physical mechanisms?

The remainder of this paper is organized as follows. Section 2 describes the datasets and reconstruction methodology. Section 3 presents the ERA5 reconstruction results and the CMIP6 evaluation. Section 4 discusses the dynamical interpretation of intermodel spread and summarizes the main findings.

2 Data and methods

2.1 Data

We use the ERA5 dataset, the fifth-generation global atmospheric reanalysis produced by the European Centre for Medium-Range Weather Forecasts (Hersbach et al. 2020), distributed via the Copernicus Climate Change Service. Our analysis focuses on the boreal winter (December–February; DJF) for the period spanning 1979 to 2014, chosen to match the historical simulations of the Coupled Model Intercomparison Project Phase 6 (CMIP6). We use (1) 500-hPa geopotential height to diagnose storm-track activity; (2) total precipitation to characterize regional hydrological changes; and (3) pressure-level air temperature to interpret storm-track variability and associated precipitation changes in relation to baroclinicity and static stability. ERA5 fields are provided on a 0.25°×0.25° latitude–longitude grid at 6-hourly resolution. All fields are bilinearly interpolated to a 1.5°×1.5° grid and subsequently aggregated to daily means.

We analyze CMIP6 simulations (Eyring et al. 2016) from two experiments: the historical and the high-emissions Shared Socioeconomic Pathway 5–8.5 scenario (SSP585; O'Neill et al., 2016). To avoid disproportionate weighting across models, we use only the first ensemble member of each model (variant label r1i1p1f1). As in ERA5, the historical simulation analysis is restricted to DJF over December 1979–February 2014, and future changes are assessed using SSP585 over DJF from December 2015–February 2100. The number of models differs between historical and SSP585 analyses due to the availability of daily output for the required variables. Based on data availability, geopotential height and total precipitation are taken from 21 models for the historical period and 19 models for SSP585. In contrast, zonal-mean temperature is

https://doi.org/10.5194/egusphere-2026-3431
Preprint. Discussion started: 25 June 2026

analyzed using a reduced subset of 20 models for the historical simulation and 16 models for the SSP585 simulation. Model-specific information is summarized in Supplementary Table 1.

2.2 Decomposition of circulation variability

Following the approach of Lau et al. (1988), we quantify changes in circulation variability using the variance of the 500-hPa geopotential height anomalies (Z'_{500}), where the anomaly is defined by removing the 1979/80–2013/14 DJF mean field (i.e., the DJF climatological mean). To isolate the transient component (Z'_T), we apply a 2–8-day Lanczos band-pass filter with a 13-day window to the height anomaly. The residual is defined as the stationary/low-frequency component (Z'_S):

$$Z'_{500}(t,\phi,\lambda) = Z'_S + Z'_T \,, \quad (1)$$

where the height anomaly is a function of time (t), latitude (ϕ), and longitude (λ). Circulation variability is measured by a 5-day running variance. The 5-day window follows the storm-track activity definition of Lau et al. (1988) and subsequent applications (e.g., Yoo et al. 2025), and is intended to provide a daily, spatial measure of synoptic disturbance amplitude. Accordingly, we define high-frequency residuals (denoted by double primes) by removing a 5-day running mean from each field:

$$Z''_{500}(t,\phi,\lambda) = Z'_{500} - \bar{Z}'^{(5)}_{500} \,, \quad (2)$$

where $\overline{(\cdot)}^{(5)}$ denotes a 5-day running mean. Combining Eqs. (1) and (2), the 5-day running variance of the total fluctuations can then be expanded as:

$$\overline{(Z''_{500})^2}^{(5)}(t,\phi,\lambda) = \overline{(Z''_S)^2}^{(5)} + \overline{(Z''_T)^2}^{(5)} + \overline{2(Z''_S Z''_T)}^{(5)} \,,$$

which can be written concisely as,

$$\mathrm{VAR}_{Z'}(t,\phi,\lambda) = \mathrm{VAR_S} + \mathrm{VAR_T} + 2\mathrm{COV} \,, \quad (3)$$

Here, $\mathrm{VAR_T}$ corresponds to the storm-track activity based on transient disturbances, while $\mathrm{VAR_S}$ represents the activity of the stationary background. The covariance term, 2COV, captures the interaction between the two components.

2.3 EOF–regression reconstruction

EOF analysis is applied independently to the zonal-mean fields of each component, so that the resulting EOFs depend only on latitude. The use of the zonal mean reflects our focus on Northern Hemispheric precipitation changes. Although the analysis could be extended to retain longitudinal structure, doing so would require a basin-scale treatment of variability and attribution of regional-scale variability and trends, which are beyond the scope of this study.

We use 90 daily values of each DJF starting on 1 December over 0°N–70°N. For the EOF–regression reconstruction, all datasets (reanalysis and CMIP6 simulations) are interpolated onto a 5°× 5° grid to provide a consistent, reduced-dimensional representation of hemispheric-scale circulation variability. This resolution is sufficient for the zonal-mean diagnostics used here and is consistent with our focus on large-scale precipitation redistribution rather than regional-scale variability and trends. Prior to the EOF calculation, each field is weighted by the square root of the cosine of latitude. The

https://doi.org/10.5194/egusphere-2026-3431
Preprint. Discussion started: 25 June 2026

associated principal component (PC) time series is obtained by projecting the daily anomaly field onto the corresponding EOF pattern. PCs are normalized to unit variance, and EOF patterns are scaled accordingly, so that the product of an EOF pattern and its PC represents the contribution of that mode to the daily field. In the analyses below, we retain the first three EOF modes because they capture nearly 90% of the total variance in the zonal-mean circulation variability (85.5% in ERA5, 88.9% in the CMIP6 historical MMM, and 88.9% in the CMIP6 SSP585 MMM). Higher-order modes explain only a small residual fraction and primarily represent weaker, more spatially complex, or dataset-specific variability. Thus, the leading three modes provide a compact basis for diagnosing the dominant hemispheric-scale storm-track response, and including additional modes is unlikely to substantially alter the main interpretation. We further verify that this truncated EOF representation faithfully captures the circulation variability from which it is derived. That is, the trend of $\mathrm{VAR}_{Z'}$ is reproduced by the three modes and their trends in ERA5 and across the CMIP6 ensembles (Supplementary Fig. 1). This supports the use of these modes as a compact and physically meaningful basis for linking circulation variability to precipitation.

To connect circulation-variability modes to precipitation, we quantify the statistical relationship between daily precipitation anomalies and the EOF PCs derived from the height-activity fields using linear regression. Specifically, precipitation anomalies $P'(t,\phi,\lambda)$ are linearly regressed onto the PCs of each component field. Using these regression coefficients, we reconstruct the component of precipitation variability that is linearly associated with the leading circulation modes as follows:

$$P'_{Reconst.}(t,\phi,\lambda) = \sum_{i\in\{S,T,Cov.\}}\sum_{k=1}^{3}\beta_{i,k}(\phi,\lambda)\mathrm{PC}_{i,k}(t)\,, \tag{4}$$

where i denotes the stationary, transient, and covariance components, k is the EOF mode index, $\beta_{i,k}$ are spatially varying regression coefficients representing the sensitivity of precipitation to each mode, and $PC_{i,k}$ are the corresponding temporal PC time series. Accordingly, the linear trend (Δ) of the reconstructed precipitation can be decomposed into the sum of each mode's contribution as:

$$\Delta P'_{Reconst.}(\phi,\lambda) = \sum_i\sum_k \beta_{i,k}(\phi,\lambda)\cdot\Delta\mathrm{PC}_{i,k}\,. \tag{5}$$

We then compute the zonal mean of the reconstructed precipitation trend to emphasize hemispheric-scale changes.

2.4 Evaluation methods

To evaluate the performance of the dynamical reconstruction framework, we calculate the pattern correlation coefficient (PCC) and the amplitude ratio (AMP) between the total ($[\Delta P']$) and reconstructed ($[\Delta P'_{Reconst.}]$) zonal mean precipitation trends (Kim et al., 2024). Here $[\cdot]$ represents the zonal mean. The PCC and AMP are defined as:

$$\mathrm{PCC} = \frac{\sum_\phi[\Delta P'_{Reconst.}](\phi)\cdot\sum_\phi[\Delta P'](\phi)\cdot\cos\phi}{\sqrt{\sum_\phi[\Delta P'_{Reconst.}]^2(\phi)\cdot\cos\phi}\sqrt{\sum_\phi[\Delta P']^2(\phi)\cdot\cos\phi}}\,, \tag{6}$$

$$\mathrm{AMP} = \frac{\sqrt{\sum_\phi[\Delta P'_{Reconst.}]^2(\phi)\cdot\cos\phi}}{\sqrt{\sum_\phi[\Delta P']^2(\phi)\cdot\cos\phi}}\,, \tag{7}$$

https://doi.org/10.5194/egusphere-2026-3431
Preprint. Discussion started: 25 June 2026

PCC measures spatial pattern similarity, while AMP compares the relative magnitude of the reconstructed trend with that of the total trend. The projection coefficient (PROJ), defined as the product of PCC and AMP,

$$\mathrm{PROJ} = \mathrm{PCC} \times \mathrm{AMP}, \tag{8}$$

measures the effective projection of the reconstructed trend onto the total precipitation trend by accounting for both spatial similarity and relative amplitude. A higher PROJ score indicates that the reconstructed trend more strongly projects onto the total trend.

https://doi.org/10.5194/egusphere-2026-3431
Preprint. Discussion started: 25 June 2026

3 Results

3.1 Evaluation of the circulation-based precipitation reconstruction

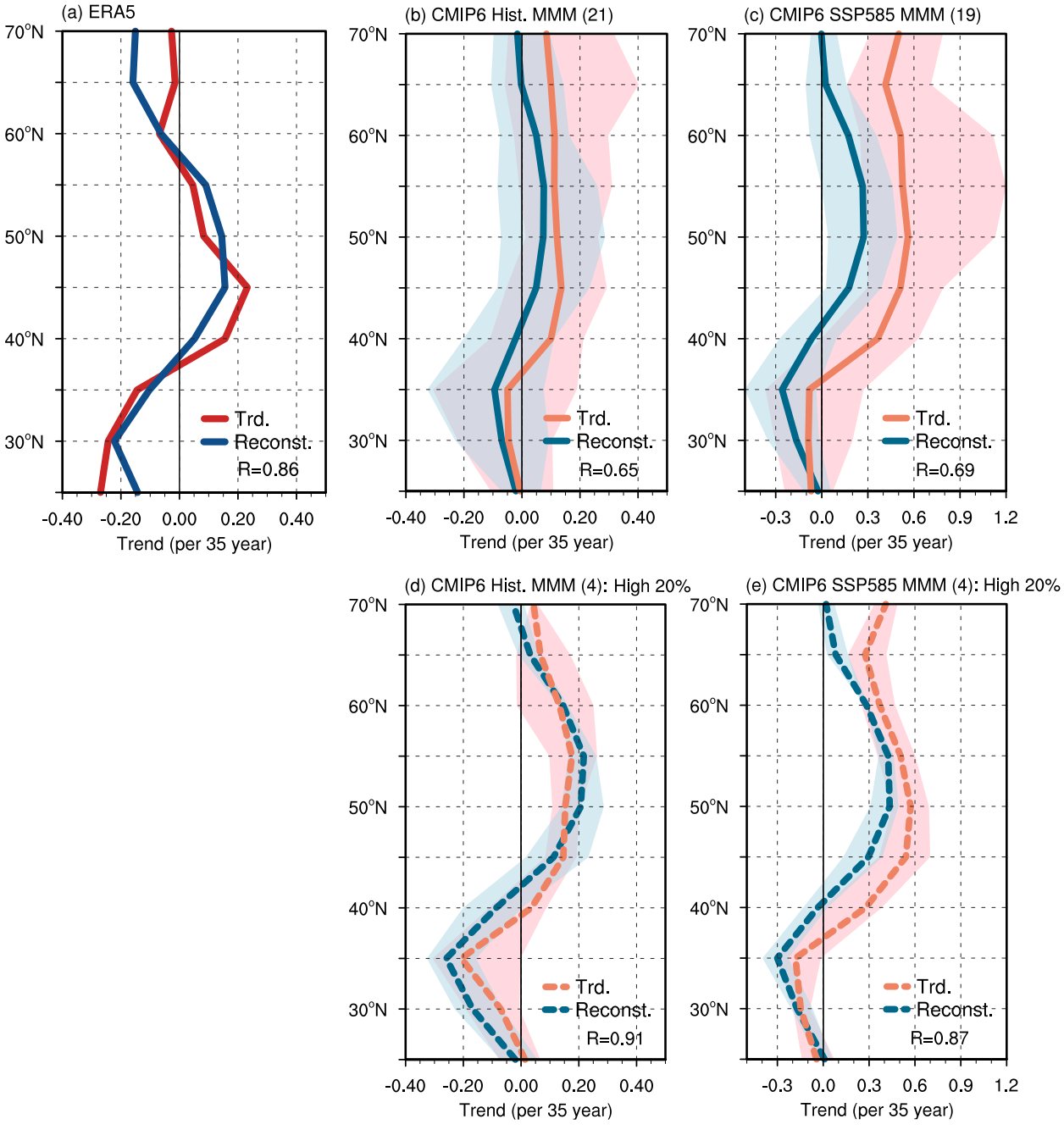

Figure 1: Zonal-mean profiles of total precipitation trends and circulation-based reconstruction. Zonal-mean profiles of total precipitation trends (orange/red lines) and circulation-based reconstructions (blue lines) for (a) ERA5 (1979–2014), (b) the CMIP6 historical multi-model mean (MMM; 21 models, 1979–2014), and (c) the CMIP6 SSP585 MMM (19 models, 2015–2100). Panels (d) and

https://doi.org/10.5194/egusphere-2026-3431
Preprint. Discussion started: 25 June 2026

(e) show the same quantities for subsets composed of the four models selected from the top ~20% ranked by PROJ score in the historical and SSP585 ensembles, respectively. Solid lines are used in (a)–(c), and dashed lines are used in (d)–(e). The reconstructions are obtained by summing all decomposed 500-hPa geopotential height (Z500) activity components. R denotes the pattern correlation coefficient between the two profiles. Shading in (b)–(e) indicates the intermodel range (minimum to maximum) across individual models.

We first assess how well the leading circulation-variability modes reconstruct multidecadal midlatitude precipitation trends. Applying the EOF–regression framework to ERA5 yields a faithful reconstruction of the DJF precipitation trend pattern (Fig. 1a). Using nine circulation modes (three EOFs each for $\mathrm{VAR_S}$, $\mathrm{VAR_T}$, and COV), the reconstruction (blue line) agrees well with the total precipitation trend (red line) in both spatial structure (PCC = 0.86) and the overall amplitude (AMP = 0.83). The reconstruction captures the meridional dipole pattern, with maximum drying near 25°N and maximum wetting near 45°N. Some disagreement remains poleward of 60°N, where the reconstructed trend indicates drying that is not evident in the observed trend. Nevertheless, the overall similarity demonstrates that a large fraction of the observed redistribution is linearly associated with a small set of leading circulation-variability modes.

We next apply the same framework to the CMIP6 historical simulations. In the historical multi-model mean (MMM; Fig. 1b), the reconstructed trend (blue line) closely matches the simulated DJF precipitation trend (orange line). Structural agreement is reasonably strong (PCC = 0.65), suggesting that the CMIP6 MMM broadly captures the dynamical linkage between circulation change and hemispheric precipitation redistribution. The reconstructed amplitude is, however, consistently weaker than the simulated trend (AMP = 0.61), particularly near 40°N and poleward of 65°N. In addition, the intermodel spread of the reconstruction (shading) is approximately 0.2–0.4 mm per 35 years, substantially exceeding the MMM trend itself (about 0.1 mm per 35 years over 45°N–65°N). This weaker reconstructed amplitude in the CMIP6 MMM than in ERA5 is broadly consistent with recent evidence that climate models tend to underestimate observed poleward storm-track migration (Chemke and Yuval 2026). Thus, even when the MMM pattern is reasonably reproduced, the magnitude of circulation-mediated precipitation change is strongly shaped by intermodel differences in the underlying circulation response. This weak amplitude, despite the reasonable agreement in the pattern, is also evident in the horizontal spatial distributions of the circulation-linked precipitation trends (Supplementary Fig. 2).

The mismatches in pattern and amplitude are reduced when the analysis is restricted to models with stronger dynamical consistency. Here, dynamical consistency is defined as the degree to which the reconstructed circulation-driven precipitation trend matches the total simulated precipitation trend, as quantified by the PROJ score (Eq. (8)). For the four models with the highest PROJ scores (Fig. 1d), the reconstructed (blue dashed line) and simulated trends (orange dashed line) agree much more closely in both pattern (PCC = 0.91) and magnitude (AMP = 1.25), and the intermodel spread is substantially reduced (shading). The improved agreement is also apparent in the spatial distribution (Supplementary Fig. 2d). Although this comparison partly reflects the PROJ-based model selection, it provides a useful diagnostic illustration of how intermodel differences can weaken the MMM reconstruction. In models where the reconstructed circulation component is more strongly aligned with the simulated precipitation trend, the reconstructed and simulated trends agree more closely, and the intermodel spread is substantially reduced.

https://doi.org/10.5194/egusphere-2026-3431
Preprint. Discussion started: 25 June 2026

In SSP585 (Fig. 1c), the reconstruction (blue line) still captures the dominant spatial structure of the total precipitation trend (orange line), but it explains a smaller fraction of the total simulated trend magnitude. Consistent with this, the SSP585 MMM exhibits reasonable structural agreement (PCC = 0.69) but a reduced amplitude (AMP = 0.45). Restricting the SSP585 MMM to the four highest-PROJ models improves the agreement (PCC = 0.87 and AMP = 0.71; Fig. 1e and Supplementary Fig. 2e), indicating that intermodel differences still contribute to the reduced amplitude in the full MMM. At the same time, part of this reduced amplitude is expected because, under strong warming, an increasing share of the total precipitation trend can arise from thermodynamic forcing rather than circulation change. For example, thermodynamic moistening can amplify precipitation, even when the large-scale flow changes only modestly. Our reconstruction, by design, retains only the portion of precipitation that covaries with the leading circulation-mode PCs. Nevertheless, the relatively high spatial agreement indicates that circulation variability continues to shape where the response occurs, even as thermodynamic forcing increasingly influences its magnitude.

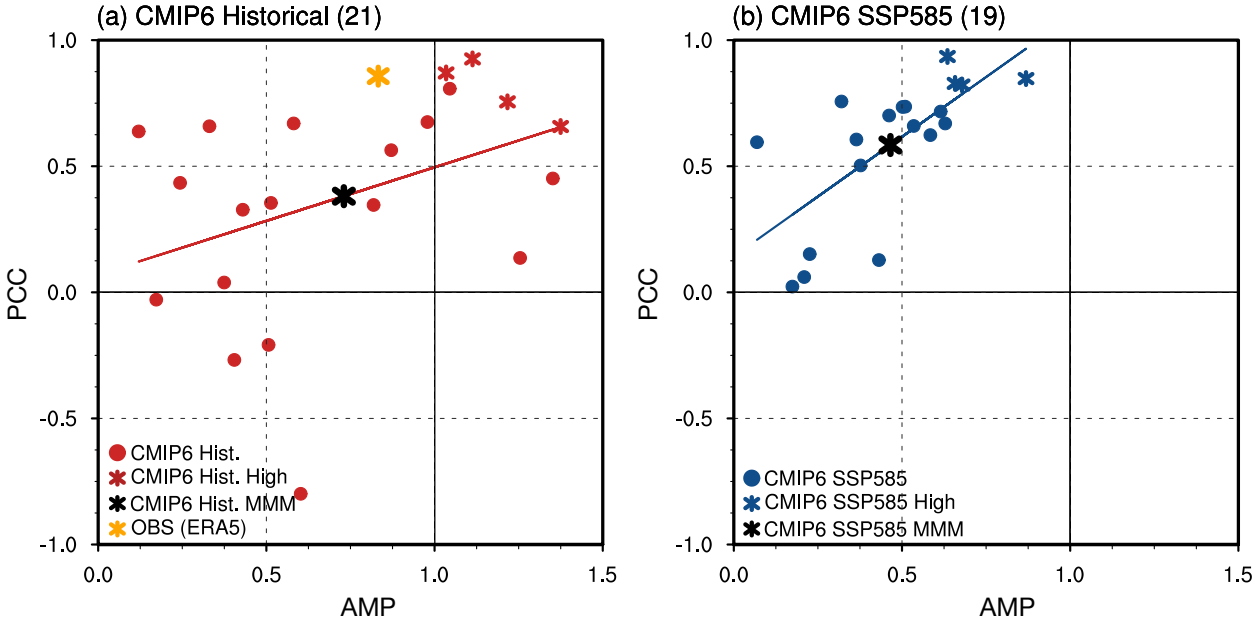

Figure 2: Phase-space relationship between pattern correlation coefficient (PCC) and relative amplitude (AMP) for circulation-based precipitation reconstruction. Results are shown for (a) CMIP6 historical simulations (21 models) and (b) CMIP6 SSP585 simulations (19 models). The y-axis denotes the pattern correlation coefficient (PCC), and the x-axis denotes the relative amplitude (AMP), defined as the ratio of the reconstruction amplitude to that of the total precipitation trend. Colored circles indicate individual CMIP6 models; colored asterisks indicate the top ~20% of models ranked by PROJ score; black asterisks denote the multi-model mean (MMM); and the yellow asterisk in (a) marks ERA5. Solid colored lines show the fitted linear relationship between PCC and AMP across models.

Figure 2 expands the comparison across CMIP6 models in PCC–AMP phase space. ERA5 (yellow asterisk in Fig. 2a) exhibits high PCC and near-unity amplitude. In CMIP6 historical simulations (Fig. 2a), the MMM (black asterisk) shows a moderate amplitude but substantially lower PCC than ERA5, while individual models display pronounced intermodel differences in reconstruction skill (red dots). The top 20% PROJ models (red asterisks; corresponding to the Fig. 1d subset)

https://doi.org/10.5194/egusphere-2026-3431
Preprint. Discussion started: 25 June 2026

cluster toward the upper-right portion of the phase space. The fitted red line indicates a positive, approximately linear relationship between PCC and AMP, suggesting that models with stronger pattern agreement also tend to recover larger reconstructed amplitudes. Under SSP585 (Fig. 2b), intermodel spread remains evident but is reduced, with models clustering more tightly (blue dots). As in the historical simulations, the top 20% PROJ models are highlighted by blue asterisks (corresponding to the Fig. 1e subset), and the fitted blue line again shows a positive PCC–AMP relationship. Compared with the historical simulations, the SSP585 ensemble spans a narrower range of amplitudes while maintaining moderate to high PCC. Overall, the positive PCC–AMP relationship indicates that models that better represent the meridional structure also tend to capture a larger fraction of the precipitation-trend amplitude. Motivated by the PCC–AMP relationship and intermodel spread, we next decompose the reconstruction into leading variability modes to identify the dominant sources of that spread.

3.2 CMIP6 model biases in shift and sharpening mechanisms

We next decompose the circulation-linked reconstruction into transient, stationary, and interaction components (Eq. (3)) to determine which dynamical contribution dominates the precipitation trend. We use the PROJ score (Eq. (8)) to compare each decomposed component directly with the total precipitation trend.

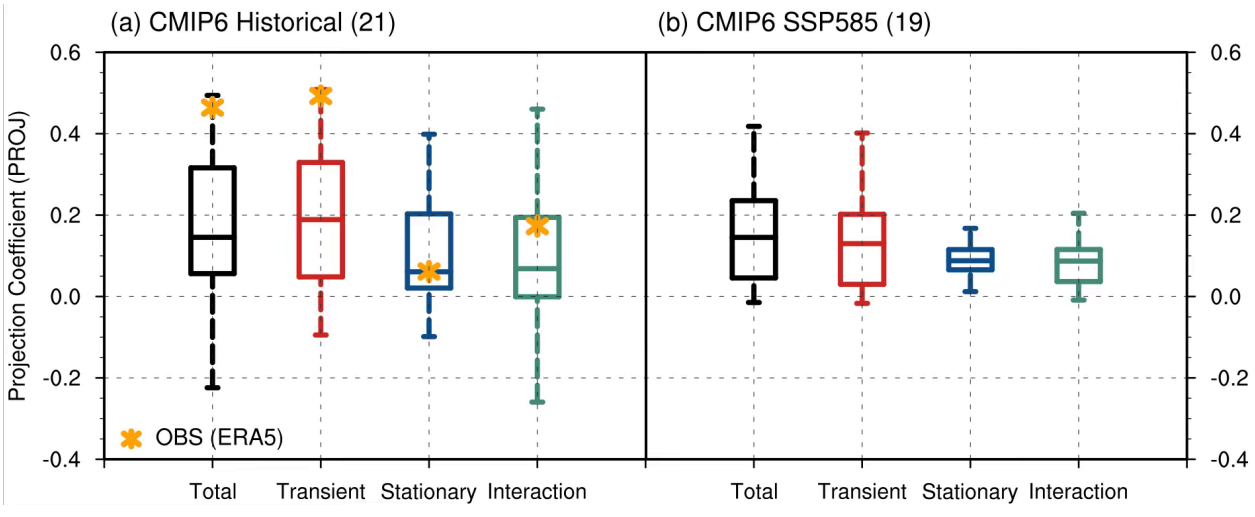

Figure 3: Projection coefficient (PROJ) scores for the total circulation-linked reconstruction and its decomposed components. Results are shown for (a) CMIP6 historical (21 models) and (b) CMIP6 SSP585 (19 models). Box plots show the intermodel distribution of PROJ for the total (black), transient (red), stationary (blue), and interaction (green) components, with the center line indicating the mean and boxes indicating the interquartile range; whiskers denote the minimum to maximum across models. Yellow asterisks mark the corresponding ERA5 values in (a).

The transient component dominates the reconstruction in ERA5 as well as in both the historical and SSP585 simulations (Fig. 3). In ERA5 (yellow asterisk in Fig. 3a), total PROJ reaches ~0.45–0.5. This is closely matched by the transient contribution (~0.5), while the stationary and interaction terms remain below ~0.2. In CMIP6, the intermodel

https://doi.org/10.5194/egusphere-2026-3431
Preprint. Discussion started: 25 June 2026

distribution of the total PROJ score is much smaller (centered near ~0.15) in both periods (black box plots), consistent with weaker reconstructed amplitude. Nevertheless, the transient term (~0.12–0.15; red box plots) still exceeds the stationary and interaction contributions (blue and green box plots). This pattern of relative importance is also evident in the spatial patterns and zonal-mean profiles (Supplementary Fig. 3), where the transient contribution dominates the reconstructed signal. Intermodel spread is substantial in both ensembles, although it is slightly reduced under SSP585 (Fig. 3), consistent with the clustering in Fig. 2. Because the transient component accounts for most of the reconstruction and exhibits substantial intermodel dispersion, the key question is which modes of transient variability contribute to the trend and whether models reproduce the same EOF-mode mixture as ERA5. Differences in the transient EOF mixture are therefore likely to be the primary source of intermodel differences in the reconstructed trend pattern and amplitude.

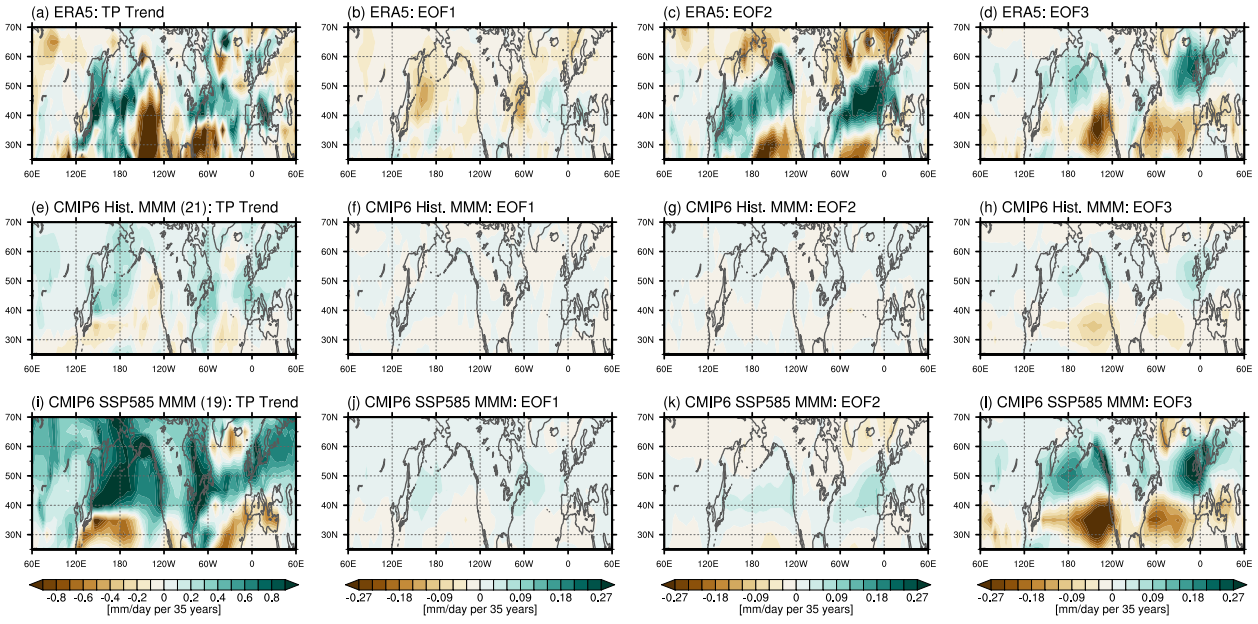

Figure 4: Spatial patterns of transient-induced total precipitation trends and their EOF-based contributions. Results are shown for (a)–(d) ERA5 (1979–2014), (e)–(h) the CMIP6 historical multi-model mean (MMM; 21 models, 1979–2014), and (i)–(l) the CMIP6 SSP585 MMM (19 models, 2015–2100). Columns show, from left to right, the transient-induced total precipitation trend and the contributions associated with EOF1, EOF2, and EOF3, respectively. Shading indicates trend magnitude (mm day^{-1} per 35 years).

Because the transient component dominates the reconstruction and shows substantial intermodel spread, we next examine how the transient-induced precipitation trend projects onto the three leading storm-track EOF modes (Fig. 4 and Supplementary Fig. 4). In ERA5, EOF1 (panels b), representing storm-track pulsing, contributes little to the total transient-induced trend. By contrast, EOF2 (panels c), capturing a meridional shift of the storm track, produces a pronounced dipole consistent with a poleward displacement of the precipitation band. EOF3 (panels d), representing meridional sharpening, contributes substantially to the narrowing and intensification of midlatitude precipitation. Together, EOF2 and EOF3 account for most of the observed transient-induced trend pattern (panels a).

https://doi.org/10.5194/egusphere-2026-3431
Preprint. Discussion started: 25 June 2026

In contrast, in the CMIP6 historical MMM (Figs. 4e–h and Supplementary Figs. 4e–h), the transient-induced precipitation trend is dominated by EOF3, while EOF1 and EOF2 make only weak contributions. This explains why the transient-induced precipitation trend is markedly weaker in the historical MMM (panels e) than in ERA5 (panels a). The relatively strong contribution of EOF3 indicates that the MMM preferentially captures the sharpening-type response, whereas the pulsing (EOF1) and poleward-shift (EOF2) signatures that are evident in ERA5 are strongly muted. Importantly, the weak EOF1 and EOF2 signals in the MMM arise from substantial intermodel cancellation; individual models exhibit widely varying, often opposite-signed trends in these two modes, whereas the EOF3 trend is comparatively consistent across models (shading in Fig. 4). As a result, EOF1 and EOF2 contribute little to the MMM, whereas EOF3 remains robust. This behavior contrasts with ERA5, where both EOF2 and EOF3 contribute substantially to the observed trend.

Similarly, under SSP585 (Figs. 4i–l and Supplementary Figs. 4i–l), the total transient-induced trend remains dominated by EOF3, while EOF1 and EOF2 continue to contribute little to the MMM response. Again, the weak MMM contribution from EOF1 and EOF2 arises from substantial intermodel spread (shading in Fig. 4). In contrast, EOF3 exhibits a more coherent trend across models and therefore remains the dominant contribution to the SSP585 MMM response.

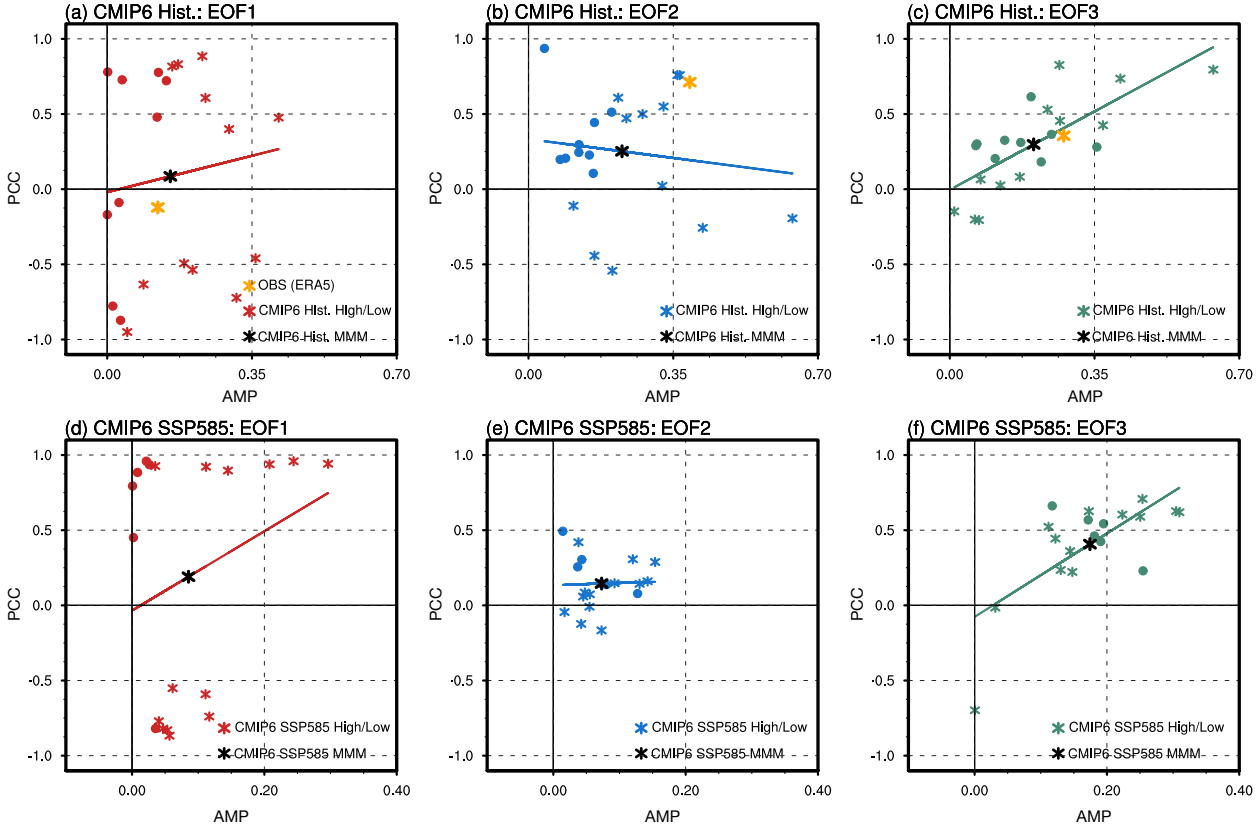

Figure 5: PCC–AMP phase space for individual EOF modes of the transient-induced total precipitation trend. Results are shown for (a)–(c) CMIP6 historical and (d)–(f) CMIP6 SSP585 simulations, displaying (a, d) EOF1, (b, e) EOF2, and (c, f) EOF3. The y-axis

https://doi.org/10.5194/egusphere-2026-3431
Preprint. Discussion started: 25 June 2026

denotes PCC and the x-axis denotes relative amplitude (AMP; reconstruction-to-original trend amplitude ratio). Colored circles indicate individual CMIP6 models, black asterisks denote the CMIP6 multi-model mean (MMM), and orange asterisks denote ERA5 values (shown in a–c). Colored asterisks mark the selected high- and low-skill model subsets used for the subsequent composite analysis, defined as the top and bottom ~30% of models ranked by PROJ score. For visualization, models located above (below) the MMM asterisk in PCC are defined as the high-skill (low-skill) subset. Solid lines show the fitted linear PCC–AMP relationship across models.

Figure 5 further shows that these weak MMM contributions from EOF1 and EOF2 arise from intermodel cancellation rather than the absence of these modes in individual simulations. In each panel, colored circles and asterisks denote individual CMIP6 models and the selected model subsets, respectively, while the black asterisk marks the MMM. In historical simulations, EOF1 (Fig. 5a) exhibits PCC values distributed around zero, with both positive and negative projections onto the total precipitation trend. This disagreement in sign leads to strong cancellation in the MMM, leaving its PCC near zero. Previous studies have similarly shown that CMIP6 models do not agree on the sign of historical storm-track pulsing trends, likely reflecting the dominant role of natural variability (Chang et al. 2012; Lee et al. 2012; Chemke et al. 2022; Campbell and Renwick 2023). EOF2 (Fig. 5b) exhibits greater sign coherence; most models yield positive PCCs, and the MMM is broadly consistent with ERA5, supporting a poleward-shift contribution to the historical trend. However, the MMM PCC remains modest relative to the intermodel spread, and the weak slope indicates that a larger EOF2 amplitude does not necessarily translate into better pattern agreement. By contrast, EOF3 (Fig. 5c) is characterized by a positive MMM PCC, a larger AMP, and a clearer positive PCC–AMP relationship, indicating that models with stronger EOF3 amplitude reproduce the sharpening pattern more consistently. This helps explain why EOF3 is retained more robustly than EOF2 in the historical MMM.

Under SSP585 (Figs. 5d–f), the intermodel behavior becomes more distinct across the three EOF-based reconstructions. EOF1 (Fig. 5d) exhibits a strongly bimodal distribution, separating into positive- and negative-PCC branches that largely cancel in the MMM, even though the positive branch tends to reach larger amplitudes. In contrast, EOF2 and EOF3 exhibit more coherent signs: EOF2 (Fig. 5e) is predominantly negative in PCC with limited amplitude, whereas EOF3 (Fig. 5f) clusters in the positive-PCC, moderate-amplitude regime and retains a clear positive slope. This suggests that understanding the sources of the spread of EOF1 and EOF2 is key to explaining the intermodel differences.

3.3 Zonal-mean temperature structure and storm-track-driven precipitation trends

To identify the physical drivers of intermodel spread in midlatitude precipitation trends, we partition the CMIP6 ensemble into high- and low-PROJ subsets. We first compare how these subsets differ in transient-induced precipitation-trend contributions under historical and SSP585 forcing (Figs. 6–7). We then examine the corresponding zonal-mean temperature fields associated with each mode (Fig. 8), as a compact measure of the large-scale thermal structure that organizes storm-track activity.

https://doi.org/10.5194/egusphere-2026-3431
Preprint. Discussion started: 25 June 2026

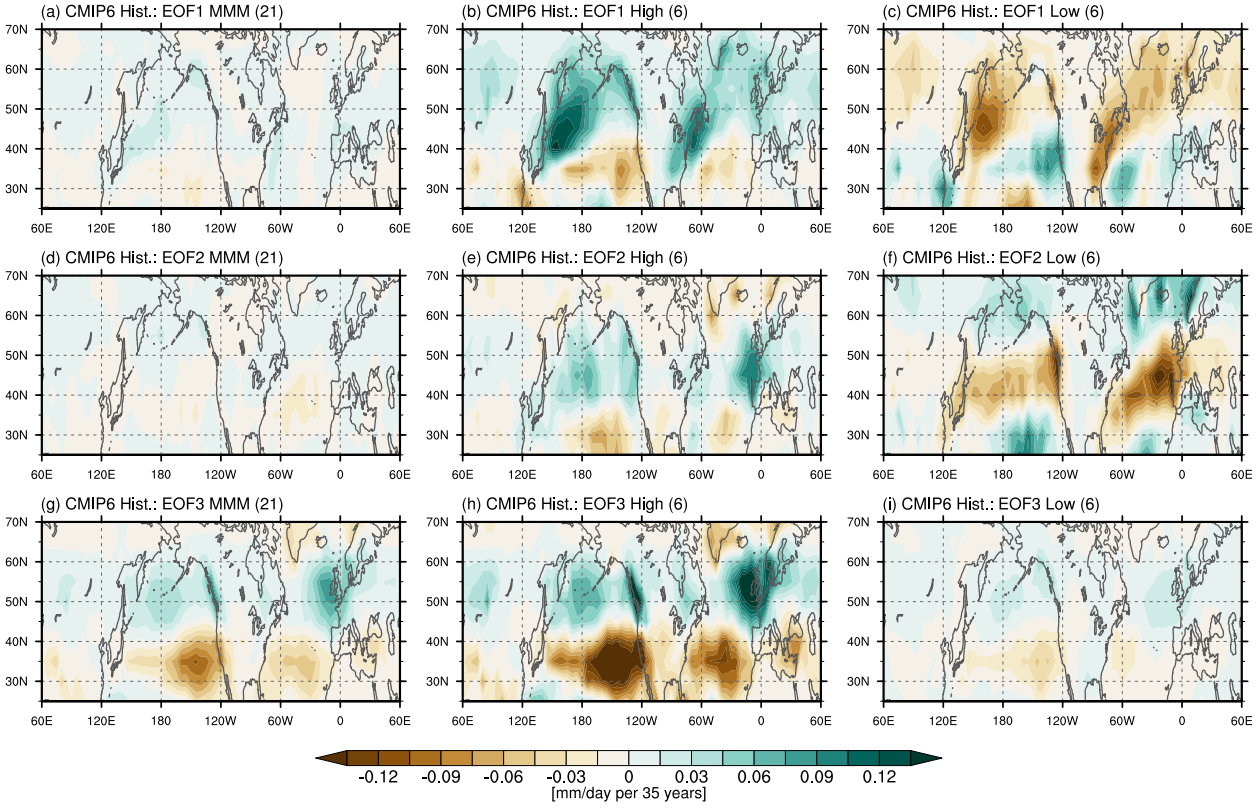

Figure 6: Spatial patterns of transient-induced precipitation trend contributions for EOF modes and PROJ-based model subsets. Maps show the transient-induced total precipitation trend contributions associated with (a)–(c) EOF1, (d)–(f) EOF2, and (g)–(i) EOF3 in CMIP6 historical simulations (1979–2014). Columns show (left) the CMIP6 historical MMM (21 models), (middle) a PROJ-based high-skill subset, and (right) a low-skill subset. For each EOF mode, the high- and low-skill subsets are defined as the top and bottom ~30% of models ranked by PROJ score (Eq. (8)) (6 out of 21 models). Numbers in parentheses indicate the number of models in each panel. Shading indicates the trend magnitude (mm day^{-1} per 35 years).

Figure 6 compares the transient-induced precipitation-trend contributions across EOF modes between the high- and low-PROJ subsets in the CMIP6 historical ensemble. The high and low subsets are defined as the top and bottom ~30% of models ranked by PROJ score. For EOF1 and EOF2 (Figs. 6a–f), the two subsets exhibit nearly opposite anomaly patterns, indicating sign disagreement in the EOF1- and EOF2-linked precipitation responses and explaining the weak MMM signal. For EOF3, by contrast, the high-PROJ subset exhibits a robust sharpening-type contribution, whereas the low-PROJ subset shows a similar pattern but with substantially weaker amplitude. A similar contrast appears under SSP585 (Fig. 7): EOF1 and EOF2 again show opposite-signed responses between the subsets, leading to strong cancellation in the MMM, while EOF3 remains comparatively coherent in pattern despite differences in amplitude. These subset-dependent precipitation responses motivate examining whether the associated thermal structures also differ systematically between the two groups.

https://doi.org/10.5194/egusphere-2026-3431
Preprint. Discussion started: 25 June 2026

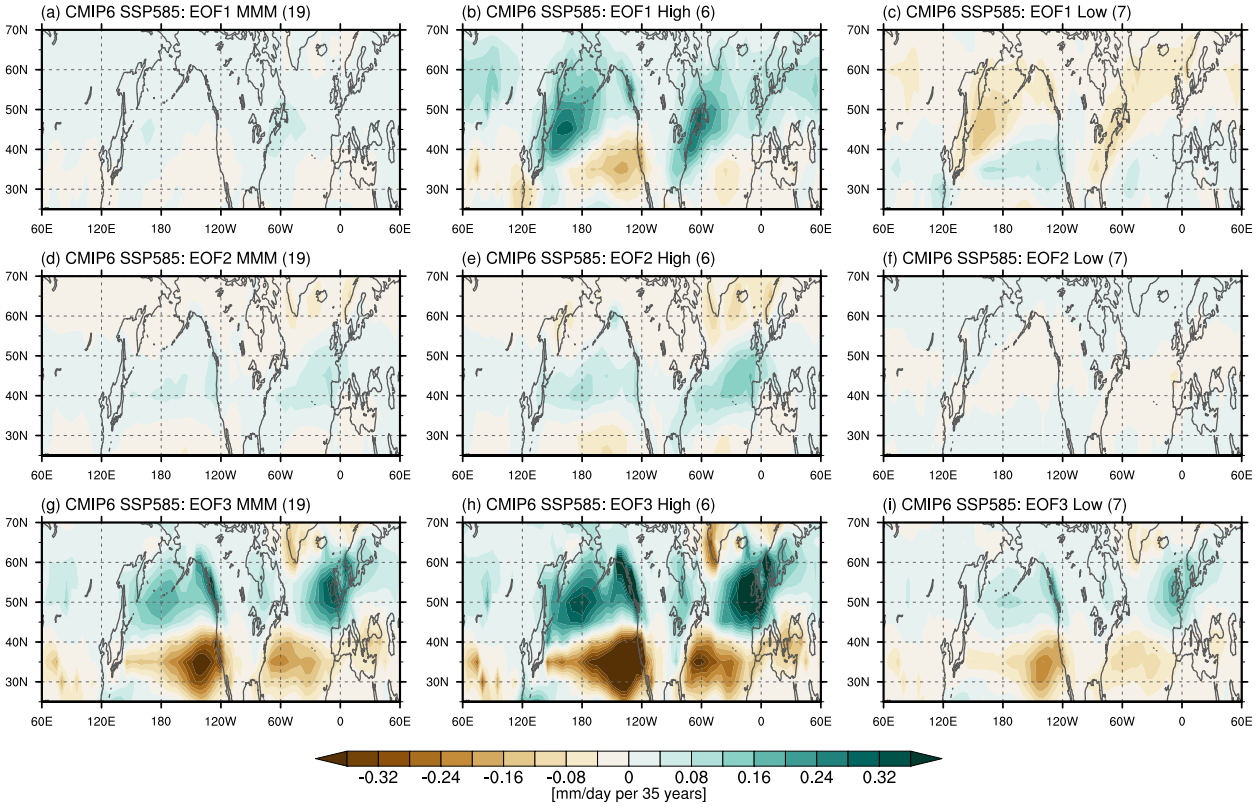

Figure 7: Spatial patterns of transient-induced precipitation trend contributions for EOF modes and PROJ-based model subsets in SSP585. Maps show the transient-induced total precipitation trend contributions associated with (a)–(c) EOF1, (d)–(f) EOF2, and (g)–(i) EOF3 in CMIP6 SSP585 simulations (2015–2100). Columns show (left) the SSP585 multi-model mean (MMM; 19 models), (middle) a PROJ-based high-skill subset, and (right) a PROJ-based low-skill subset. For each EOF mode, the high- and low-skill subsets are defined as the top and bottom ~30% of models ranked by PROJ score (Eq. (8)); numbers in parentheses indicate the number of models in each panel. Shading indicates the trend magnitude (mm day^{-1} per 35 years).

Figure 8 examines the physical background of the PROJ-based model separation by showing the high-minus-low-PROJ difference in zonal-mean temperature trends. For EOF1 (Fig. 8a), which represents storm-track pulsing, high-PROJ models exhibit weaker lower-tropospheric warming at high latitudes than low-PROJ models. By enhancing the meridional temperature gradient near 45°N, this structure favors stronger baroclinic growth, thereby increasing transient-eddy activity and the associated precipitation response. For EOF2 (Fig. 8b), associated with meridional storm-track displacement, the cold anomaly centered near 45°N indicates a redistribution of baroclinicity in latitude. Enhanced baroclinicity on the subtropical flank and reduced baroclinicity on the subpolar flank lead to an equatorward displacement of the storm track. For EOF3 (Fig. 8c), associated with storm-track sharpening, high-PROJ models show weaker warming in the high-latitude lower troposphere, but relatively stronger warming in the high-latitude upper troposphere and midlatitude troposphere. This structure sharpens the meridional temperature gradient near 45°N while weakening it near 30°N, concentrating baroclinicity within a narrower latitude band. In addition, enhanced upper-tropospheric warming at high latitudes is consistent with increased tropospheric static stability, which can further suppress baroclinic eddy growth outside the storm-track core.

https://doi.org/10.5194/egusphere-2026-3431
Preprint. Discussion started: 25 June 2026

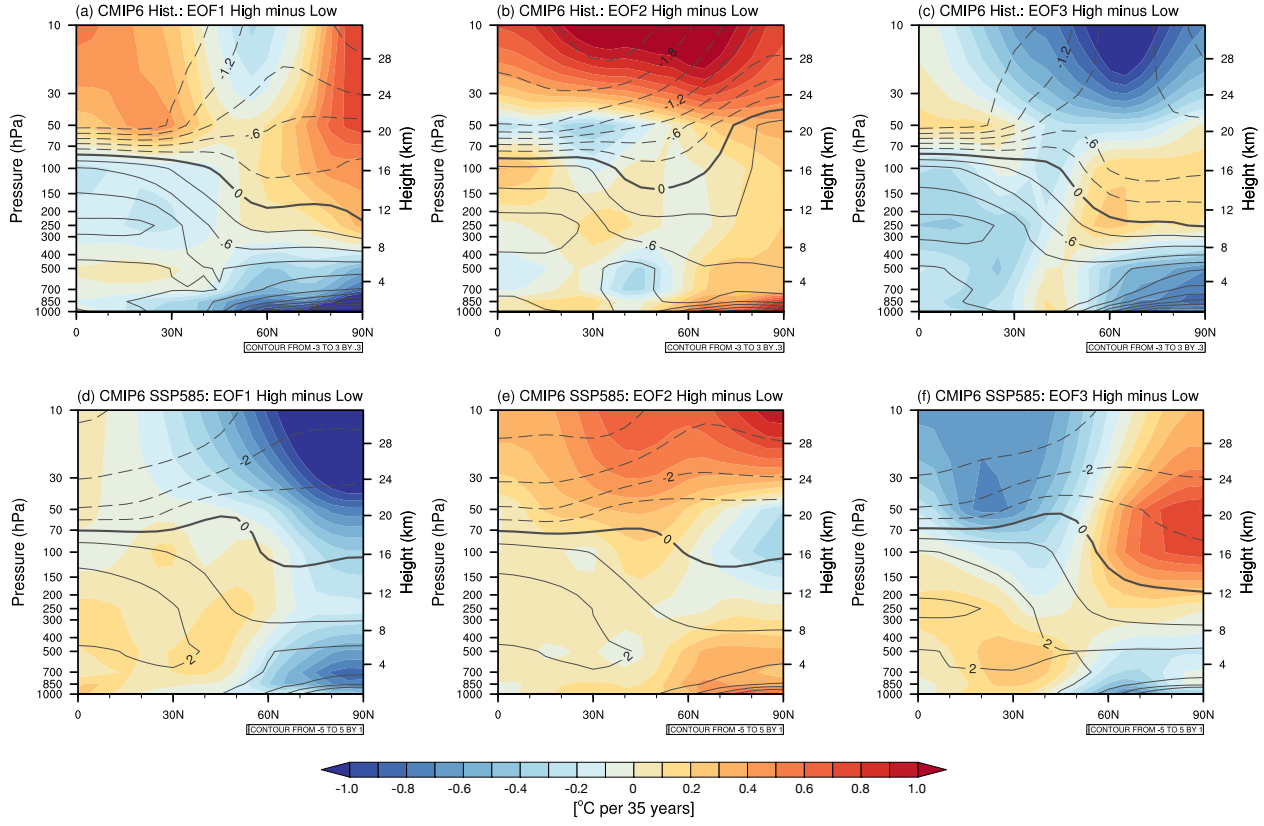

Figure 8: Zonal-mean temperature trend differences between the high- and low-PROJ model subsets in the CMIP6 historical and SSP585 simulations. Shading denotes the high-minus-low difference in temperature trends (°C per 35 years), and contours indicate the zonal-mean temperature trend of the low-PROJ subset. The upper panels show the CMIP6 historical simulations for the model groups defined by PROJ-based reconstruction skill for (a) EOF1, (b) EOF2, and (c) EOF3, consistent with the grouping used in Fig. 6. The lower panels show the corresponding CMIP6 SSP585 simulations for (d) EOF1, (e) EOF2, and (f) EOF3, consistent with the grouping used in Fig. 7. These differences highlight the latitude–height thermal structures associated with EOF-dependent storm-track responses.

As a result, high-PROJ models show a more localized and intensified storm track, and consequently a sharpened precipitation response (Fig. 6). Under SSP585 (Figs. 8d–f), the thermal structures are broadly similar to those in the historical simulations, with the same mode-dependent contrasts in meridional temperature gradients and tropospheric warming patterns. This suggests that the associated storm-track responses remain dynamically consistent under stronger warming. This interpretation is consistent with Shaw et al. (2016), who emphasized that storm-track responses to climate change arise from the competing influences of different components of the temperature response, as well as with Priestley et al. (2023), who showed that CMIP6 Northern Hemisphere storm-track biases are closely linked to biases in atmospheric temperature gradients arising from coupled-model SST errors. It is also consistent with recent work showing that enhanced North Pacific winter storm-track activity is associated with subtropical tropospheric warming and a strengthened midlatitude meridional temperature gradient (Chemke and Yuval 2026).

https://doi.org/10.5194/egusphere-2026-3431
Preprint. Discussion started: 25 June 2026

4 Discussion and Conclusions

The present framework provides a physically interpretable decomposition of precipitation change by separating the relative roles of transient, stationary, and interaction components, and by further partitioning transient variability into pulsing-, shift-, and sharpening-type storm-track responses. Using this framework, we show that a substantial fraction of multidecadal midlatitude precipitation redistribution can be explained by a small set of leading circulation-variability modes, with transient (storm-track) variability providing the dominant contribution. Across both ERA5 and CMIP6, the reconstructed precipitation trends reveal a robust meridional structure that can be decomposed into distinct modal contributions corresponding to pulsing, meridional shifting, and sharpening of storm-track activity. While the overall spatial pattern of precipitation change is broadly captured, substantial intermodel spread arises from differences in the relative contributions and signs of these modes. In particular, the pulsing- and shifting-related modes (EOF1–EOF2) exhibit large dispersion and frequent sign disagreement across models, whereas the sharpening-related mode (EOF3) is more consistently represented. These differences persist under SSP585, indicating that uncertainty in future precipitation redistribution is closely tied to how models simulate changes in storm-track variability.

The modal decomposition isolates which EOF modes contribute to the intermodel disagreement and whether the spread arises from differences in modal amplitude, sign, or circulation–precipitation coupling. Because EOF1 and EOF2 exhibit substantial intermodel sign differences, their contributions are strongly damped in the ensemble mean through cancellation, leading to an apparent dominance of EOF3. This does not necessarily imply that storm-track sharpening is the physically preferred response. Rather, the multi-model mean obscures competing mechanisms by averaging across inconsistent EOF mode mixtures. The reconstruction framework isolates these contributions and reveals that discrepancies between models arise primarily from differences in how transient-eddy variability projects onto these leading modes of circulation variability. However, caution is warranted because the reconstructed precipitation trends in CMIP6 models are systematically weaker than those in ERA5. This discrepancy highlights a limitation of the present framework when interpreting future precipitation projections, as models underestimate the strength of the circulation–precipitation coupling.

The framework further links these intermodel differences to physically interpretable variations in the background thermal structure. The sensitivity of the reconstructed precipitation response depends on how warming projects onto the midlatitude baroclinic zone. Temperature changes can either displace or sharpen the meridional temperature gradient within the storm-track latitude band, while also altering the vertical stratification of the troposphere. These effects regulate baroclinic instability and thereby modulate the amplitude, latitude, and structure of transient-eddy activity. These results, therefore, indicate that differences in the zonal-mean thermal structure across models provide a key constraint on whether storm-track responses manifest as shift-like or sharpening-like changes. Such intermodel differences in zonal-mean temperature structure likely arise from variations in climate sensitivity and the representation of key feedback processes, including cloud-radiative feedback, ocean heat uptake, and coupled air–sea interactions that shape the spatial pattern of warming. In particular, differences in how models distribute warming between the tropics and extratropics, as well as in the

https://doi.org/10.5194/egusphere-2026-3431
Preprint. Discussion started: 25 June 2026

vertical structure of tropospheric warming, can lead to systematic differences in meridional temperature gradients and, in turn, in the simulated storm-track response.

Similar to the strategy of Chemke and Yuval (2026), which constrains storm-track shifts using observational evidence, the present framework enables constraints to be applied at the level of individual EOF modes. In particular, observationally constrained estimates of the relative contributions of the shift and sharpening modes could be used to weight the future projections. Because each EOF mode represents a distinct form of storm-track reorganization, constraining their amplitudes and signs offers a more process-oriented pathway to reducing uncertainty than approaches based solely on aggregate storm-track diagnostics. This distinction is especially relevant because the spatial pattern of precipitation redistribution remains strongly linked to circulation changes, whereas the magnitude of precipitation change under strong warming may also reflect additional moisture-related effects that are not explicitly separated in the present framework.

A methodological limitation of this study is that the EOF–regression framework does not explicitly separate thermodynamic contributions from circulation-related precipitation changes. The reconstruction diagnoses precipitation variability linearly associated with leading storm-track and circulation modes, rather than performing a full dynamic–thermodynamic decomposition. Therefore, the residual between the total and reconstructed precipitation trends should not be interpreted as a purely thermodynamic component, because it may also include nonlinear circulation–precipitation interactions, regional processes outside the zonal-mean framework, and model-specific biases. Accordingly, the SSP585 results should be viewed as the response of the circulation-related reconstruction under strong warming, while a scenario-dependent separation of dynamic and thermodynamic contributions remains an important direction for future work.

Finally, although the present analysis focuses on zonal-mean structure, the framework can be naturally extended to basin-scale diagnostics. Retaining longitudinal structure in the EOF decomposition would allow the identification of basin-specific storm-track modes and their associated precipitation responses, enabling a more detailed assessment of regional mechanisms such as Pacific versus Atlantic variability or the influence of localized SST patterns within individual basins. In particular, warming patterns near western boundary currents, such as the Kuroshio and Gulf Stream, may exert an important control on regional storm-track shifts and sharpening responses. These regions are characterized by strong meridional temperature gradients and reduced static stability associated with warm ocean currents, conditions that enhance baroclinicity and help anchor climatological storm tracks (e.g., Hoskins and Valdes 1990; Nakamura and Shimpo 2004; Seo et al. 2023). Incorporating such a longitudinal structure would, therefore, provide a more complete picture of how regional circulation changes contribute to global precipitation redistribution and would allow more direct comparison with observed basin-scale storm-track behavior. This represents a promising direction for future work, particularly for understanding regional hydroclimate impacts and improving the evaluation of climate-model circulation responses at finer spatial scales.

https://doi.org/10.5194/egusphere-2026-3431
Preprint. Discussion started: 25 June 2026

Data availability

The ERA5 reanalysis is available from the Copernicus Climate Data Store (https://cds.climate.copernicus.eu/datasets/) and the CMIP6 data supporting the findings of this study are available via the Earth System Grid Federation (ESGF) nodes (https://esgf.github.io/nodes.html).

Author contributions

HRK performed data curation, formal analysis, investigation, visualization, and writing (original draft preparation, review and editing). CY performed conceptualization, investigation, project administration, supervision and writing (review and editing). HS and BMK reviewed and edited the manuscript.

Competing interests

The authors have no competing interests to disclose.

Disclaimer

Copernicus Publications adds a standard disclaimer: "Copernicus Publications remains neutral with regard to jurisdictional claims made in the text, published maps, institutional affiliations, or any other geographical representation in this paper. While Copernicus Publications makes every effort to include appropriate place names, the final responsibility lies with the authors. Views expressed in the text are those of the authors and do not necessarily reflect the views of the publisher." Please feel free to add disclaimer text at your choice, if applicable.

Acknowledgements

C.Y. acknowledges support from Ewha Global Excellence Program of Ewha Womans University. H.S. acknowledges support from US National Science Foundation grants (OCE-2148120, OCE-2022846) and the Uehiro Center for the Advancement of Oceanography (UC·AO) at the University of Hawai'i at Mānoa.

Financial support

This study was supported by the Korea Meteorological Administration Research and Development Program (grant RS-2025-02313090 and KMA2018-00321).

https://doi.org/10.5194/egusphere-2026-3431
Preprint. Discussion started: 25 June 2026

References

Barnes, E. A., and L. Polvani, 2013: Response of the midlatitude jets, and of their variability, to increased greenhouse gases in the CMIP5 models. *Journal of Climate*, **26**, 7117–7135, https://doi.org/10.1175/JCLI-D-12-00536.1.

Blackmon, M. L., Y. Lee, and J. M. Wallace, 1984: Horizontal structure of 500 mb height fluctuations with long, intermediate and short time scales. *Journal of Atmospheric Sciences*, **41**, 961–980, https://doi.org/10.1175/1520-0469(1984)041<0961:HSOMHF>2.0.CO;2.

Campbell, I., and J. A. Renwick, 2023: Southern Hemisphere storm tracks and large-scale variability: What do the latest reanalyses say? *Journal of Climate*, **36**, 5549–5567, https://doi.org/10.1175/JCLI-D-22-0726.1.

Chang, E. K., Y. Guo, and X. Xia, 2012: CMIP5 multimodel ensemble projection of storm track change under global warming. *Journal of Geophysical Research: Atmospheres*, **117**, https://doi.org/10.1029/2012JD018578.

Chemke, R., L. Zanna, C. Orbe, L. T. Sentman, and L. M. Polvani, 2022: The future intensification of the North Atlantic winter storm track: The key role of dynamic ocean coupling. *Journal of Climate*, **35**, 2407–2421, https://doi.org/10.1175/JCLI-D-21-0407.1.

Chemke, R., and J. Yuval, 2026: Climate change shifts the North Pacific storm track polewards. *Nature*, **649**, 626–630, https://doi.org/10.1038/s41586-025-09895-y.

Deng, Y., and T. Jiang, 2011: Intraseasonal modulation of the North Pacific storm track by tropical convection in boreal winter. *Journal of Climate*, **24**, 1122–1137, https://doi.org/10.1175/2010JCLI3676.1.

Eyring, V., S. Bony, G. A. Meehl, C. A. Senior, B. Stevens, R. J. Stouffer, and K. E. Taylor, 2016: Overview of the Coupled Model Intercomparison Project Phase 6 (CMIP6) experimental design and organization. *Geoscientific Model Development*, **9**, 1937–1958, https://doi.org/10.5194/gmd-9-1937-2016.

Harvey, B., P. Cook, L. Shaffrey, and R. Schiemann, 2020: The response of the Northern Hemisphere storm tracks and jet streams to climate change in the CMIP3, CMIP5, and CMIP6 climate models. *Journal of Geophysical Research: Atmospheres*, **125**, e2020JD032701, https://doi.org/10.1029/2020JD032701.

Held, I. M., and B. J. Soden, 2006: Robust responses of the hydrological cycle to global warming. *Journal of Climate*, **19**, 5686–5699, https://doi.org/10.1175/JCLI3990.1.

Hersbach, H., and Coauthors, 2020: The ERA5 global reanalysis. *Quarterly Journal of the Royal Meteorological Society*, **146**, 1999–2049, https://doi.org/10.1002/qj.3803.

Hoskins, B. J., and K. I. Hodges, 2002: New perspectives on the Northern Hemisphere winter storm tracks. *Journal of the Atmospheric Sciences*, 59, 1041–1061, https://doi.org/10.1175/1520-0469(2002)059<1041:NPOTNH>2.0.CO;2.

Kim, M., C. Yoo, and H. Kim, 2024: Process evaluation of subseasonal North Atlantic Oscillation prediction in the ECMWF ensemble forecast system. *Geophysical Research Letters*, **51**, e2024GL111291, https://doi.org/10.1029/2024GL111291.

https://doi.org/10.5194/egusphere-2026-3431
Preprint. Discussion started: 25 June 2026

Lau, N.-C., 1988: Variability of the observed midlatitude storm tracks in relation to low-frequency changes in the circulation pattern. *Journal of Atmospheric Sciences*, **45**, 2718–2743, https://doi.org/10.1175/1520-0469(1988)045<2718:VOTOMS>2.0.CO;2.

Lee, S.-S., J.-Y. Lee, B. Wang, K.-J. Ha, K.-Y. Heo, F.-F. Jin, D. M. Straus, and J. Shukla, 2012: Interdecadal changes in the storm track activity over the North Pacific and North Atlantic. *Climate Dynamics*, **39**, 313–327, https://doi.org/10.1007/s00382-011-1188-9.

Nakamura, H., and A. Shimpo, 2004: Seasonal variations in the Southern Hemisphere storm tracks and jet streams as revealed in a reanalysis dataset. *Journal of Climate*, 17, 1828–1844, https://doi.org/10.1175/1520-0442(2004)017<1828:SVITSH>2.0.CO;2.

Newman, M., G. N. Kiladis, K. M. Weickmann, F. M. Ralph, and P. D. Sardeshmukh, 2012: Relative Contributions of Synoptic and Low-Frequency Eddies to Time-Mean Atmospheric Moisture Transport, Including the Role of Atmospheric Rivers. J. Climate, 25, 7341–7361, https://doi.org/10.1175/JCLI-D-11-00665.1.

O'Neill, B. C., and Coauthors, 2016: The Scenario Model Intercomparison Project (ScenarioMIP) for CMIP6. *Geoscientific Model Development*, **9**, 3461–3482, https://doi.org/10.5194/gmd-9-3461-2016.

Peixoto, J. P., and A. H. Oort, 1992: Physics of Climate. American Institute of Physics Melville, NY, 520 pp.

Priestley, M. D., D. B. Stephenson, A. A. Scaife, D. Bannister, C. J. Allen, and D. Wilkie, 2023: Return levels of extreme European windstorms, their dependency on the North Atlantic Oscillation, and potential future risks. *Natural Hazards and Earth System Sciences*, **23**, 3845–3861, https://doi.org/10.5194/nhess-23-3845-2023.

Seager, R., N. Naik, and G. A. Vecchi, 2010: Thermodynamic and dynamic mechanisms for large-scale changes in the hydrological cycle in response to global warming. *Journal of Climate*, **23**, 4651–4668, https://doi.org/10.1175/2010JCLI3655.1.

Seager, R., and Coauthors, 2014: Dynamical and thermodynamical causes of large-scale changes in the hydrological cycle over North America in response to global warming. *Journal of Climate*, **27**, 7921–7948, https://doi.org/10.1175/JCLI-D-14-00153.1.

Seo, H., and Coauthors, 2023: Ocean mesoscale and frontal-scale ocean–atmosphere interactions and influence on large-scale climate: A review. *Journal of climate*, 36, 1981–2013, https://doi.org/10.1175/JCLI-D-20-0982.1.

Shaw, T., and Coauthors, 2016: Storm track processes and the opposing influences of climate change. *Nature Geoscience*, **9**, 656–664, https://doi.org/10.1038/ngeo2783.

Simpson, I. R., R. Seager, M. Ting, and T. A. Shaw, 2016: Causes of change in Northern Hemisphere winter meridional winds and regional hydroclimate. *Nature Climate Change*, **6**, 65–70, https://doi.org/10.1038/nclimate2783.

Simpson, I. R., K. A. McKinnon, F. V. Davenport, M. Tingley, F. Lehner, A. Al Fahad, and D. Chen, 2021: Emergent constraints on the large-scale atmospheric circulation and regional hydroclimate: Do they still work in CMIP6 and how much can they actually constrain the future? *Journal of Climate*, **34**, 6355–6377, https://doi.org/10.1175/JCLI-D-21-0055.1.

https://doi.org/10.5194/egusphere-2026-3431
Preprint. Discussion started: 25 June 2026

Trenberth, K. E., A. Dai, R. M. Rasmussen, and D. B. Parsons, 2003: The changing character of precipitation. *Bulletin of the American Meteorological Society*, **84**, 1205–1218, https://doi.org/10.1175/BAMS-84-9-1205.

Wettstein, J. J., and J. M. Wallace, 2010: Observed patterns of month-to-month storm-track variability and their relationship to the background flow. *Journal of the Atmospheric Sciences*, **67**, 1420–1437, https://doi.org/10.1175/2009JAS3194.1.

Yin, J. H., 2005: A consistent poleward shift of the storm tracks in simulations of 21st century climate. *Geophysical Research Letters*, **32**, https://doi.org/10.1029/2005GL023684.

Yoo, C., D. Jin, S. Lee, and D. Kim, 2025: A comparison of the meridional meandering of extratropical precipitation during boreal winter: eddy momentum flux versus Eulerian storm tracks. *npj Climate and Atmospheric Science*, **8**, 104, https://doi.org/10.1038/s41612-025-00992-3.

Zappa, G., L. C. Shaffrey, K. I. Hodges, P. G. Sansom, and D. B. Stephenson, 2013: A multimodel assessment of future projections of North Atlantic and European extratropical cyclones in the CMIP5 climate models. *Journal of Climate*, **26**, 5846–5862, https://doi.org/10.1175/JCLI-D-12-00573.1.